Intensity-Modulated Photocurrent Spectroscopy Measurements of High-Efficiency Perovskite Solar Cells

Ganga R. Neupane[1,2], Susanna M. Thon[2], Sheng Fu[3], Zhaoning Song[3], Yanfa Yan[3], and Behrang H. Hamadani[1, *]

[1]Engineering Laboratory, National Institute of Standard & Technology, Gaithersburg, MD 20899, USA
[2]Department of Electrical and Computer Engineering, Johns Hopkins University, Baltimore, MD 21218, USA
[3]Department of Physics and Astronomy and Wright Center for Photovoltaics Innovation and Commercialization, The University of Toledo, Toledo, OH 43606, USA
*Corresponding Author

Abstract

Frequency domain characterization has long served as an important method for the examination of diverse kinetic processes that occur in solar cells. In this study, we have investigated the dynamic response of high-efficiency perovskite solar cells utilizing ultralow intensity-modulated photocurrent spectroscopy (IMPS). Distinctive IMPS attributes were only detected as a result of this low-intensity modulation, and their evolution under light and voltage bias was investigated in detail. We generally observed only two arcs in the Q-plane plots and attributed the smaller, low-frequency arc to trap-dominated charge transport in the device. Light and voltage bias dependent measurements confirm this attribution. An equivalent circuit model was used to better understand the features and trends of these measurements and validate our physical interpretation of the results. Additionally, we tracked the IMPS response of one of the cells over time and show that a slow degradation impacts the size and attributes of the low frequency arc. Finally, we find that changes in the IMPS response correlate closely with the current vs voltage characteristics of the devices.

TOC Graphic

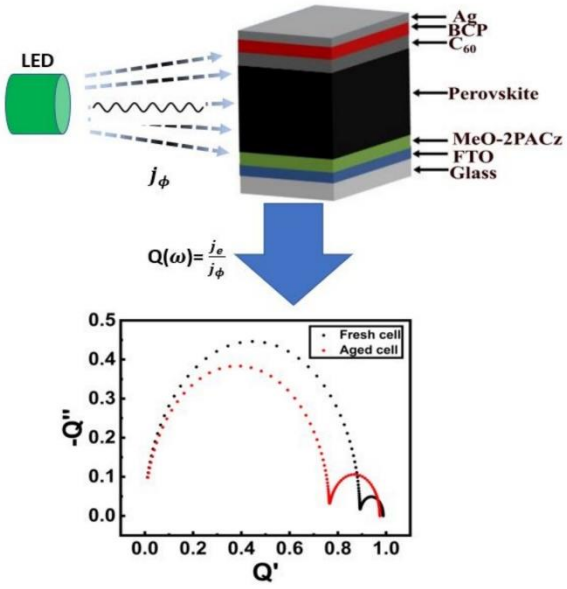

Perovskite solar cells (PSCs) have demonstrated impressive power conversion efficiencies (PCEs) of more than 26% through device optimization and interfacial passivation strategies.[1–3] These advancements could soon make PSCs a viable replacement for the more labor- and energy-intensive silicon or gallium arsenide photovoltaic (PV) technologies. Despite their rapid progress in efficiency enhancement, these solar cells remain far from large-scale commercialization due to their stability issues. Lack of stability under normal operating conditions in extended usage periods has been of particular concern within the PV community.[4,5] One effective and essential approach to improving stability is to encapsulate the device. While encapsulation serves to mitigate the detrimental effects of external factors such as oxygen, moisture, and ultraviolet light, intrinsic issues such as ion migration and carrier recombination at the interfaces and bulk of the perovskite material remain a challenge.

The perovskite electronic structure is interconnected by relatively weak interactions such as ionic bonds, hydrogen bonds, and van der Waals forces compared to strong covalent bonds in c-Si.[6] Consequently, even modest stressors can stimulate various types of defects.[7] For example, the migration and accumulation of ions at interfaces can result in nonradiative charge carrier recombination losses in PSCs. In addition to mobile ionic species, trap-mediated nonradiative recombination also constitutes a significant loss mechanism in these devices.[8] In spite of these findings, several studies have also shown that ion migration may exhibit self-passivating attributes and facilitate strain relaxation.[9,10] It has been observed that while ion migration is an important and naturally-occurring phenomenon, its action can be hindered by factors such as low ion mobility or a low number of mobile species.[9] Thus, a comprehensive investigation of charge transport pathways utilizing dynamic experimental techniques[11] such as time-resolved photoluminescence, transient photocurrent and photovoltage, thermal admittance spectroscopy, impedance spectroscopy, and intensity modulated photocurrent spectroscopy (IMPS) to detect and analyze these kinetics within PSCs is of paramount significance. In IMPS, the ac photogenerated current amplitude and phase are measured in response to excitation by a low-intensity, modulated illumination source over a range of frequencies. Time-dependent processes that affect the movement of photocarriers within the device structure show up as features in the frequency-dependent plots of the amplitude or phase of the current. Investigating these features can be a valuable approach to characterizing the processes that link the electrical and optical responses of the device.[12–14]

In recent years, efforts have been made to better quantify IMPS measurements through an important parameter called the IMPS transfer function.[12,15] The transfer function (Q), derived directly from IMPS measurements, establishes the complex-plane, ac photocurrent response of a solar cell normalized by the incident photon flux, with the x-axis representing the real component of Q, labeled as Q′, and the y-axis representing the imaginary component of Q, labeled as Q″, and usually plotted as -Q″. The Nyquist-style Q′-Q″ IMPS plots contain all the frequency-domain information that is captured in the photocurrent amplitude and phase measurements, normalized by the intensity of the excitation light source and expressed as a unitless quantum efficiency equivalent quantity (i.e., electrons per photon) with a theoretical maximum value of unity along each axis. Therefore, Q-plane plots present a very compact and powerful tool to detect any type of anomalies or interesting features in the photo-response of a fully processed solar cell. Furthermore, Q plots can be modeled by an equivalent circuit model (ECM), thereby facilitating the understanding of some of the underlying physical processes. The ECM contains different electrical

parameters, including capacitances and resistances, whose coupling is associated with different characteristic processes.

Multiple investigations have harnessed frequency-dependent techniques to probe PSCs, revealing different attributes associated with the processes.[16–19] For instance, the low-frequency limit of the IMPS transfer function correlates with the differential external quantum efficiency (EQE) of the solar cell.[17] This limit can be obtained by finding the low-frequency intercept at the Q′-axis, which reveals valuable information about the steady-state photocurrent generation by the device. There are also a variety of other low-frequency IMPS features that are generally understood to originate from ion-mediated capacitive effects. Furthermore, a variety of intermediate and high-frequency features have been reported in PSCs, corresponding to various interfacial and bulk recombination or trapping phenomena.[18–20] However, there are still significant disagreements in the literature on what IMPS features reveal about carrier dynamics and recombination losses in these devices. Furthermore, additional studies are needed to understand whether long-term degradation of PSCs can be tracked by changes in the IMPS transfer function.

In the present study, we have investigated the Q-plane features of an efficient and relatively air-stable PSC (PCE: ≈ 21 %) utilizing the IMPS technique and modeled the findings with the help of a recently proposed ECM. This simple model and other extensions of it sufficiently captures the various features of the IMPS plots and allows us to compare how internal resistance and capacitance elements change with light and voltage bias for both fresh and aged cells. In other recent studies, a diffusion-recombination model has also been proposed and used to analyze the IMPS spectra especially for extracting charge carrier diffusion parameters.[21,22] However, for this comparative study, we focus on the ECM and explanation of the changes from the circuit elements' perspective.[23] The device was fabricated following a reported method[24] with a structure shown in Fig. 1a. The measurement results reported here were typical of all the solar cells fabricated using the described procedure outlined in the Supplemental Information and the measurement results are consistently reproducible with additional detail in the Supplemental. To accentuate several interesting characteristics of the IMPS measurements, we utilized an ultralow-intensity modulation source and additional sources of steady-state light bias (LB) and forward voltage bias (VB) to examine the effect of added carriers on the features of the measured IMPS transfer function. After an initial set of measurements on fresh cells, we tracked the changes in the Q-plane plots over a period of about 8 weeks, as the cells' performance was allowed to slowly degrade in the ambient room environment (in the presence of room light and at a relatively constant temperature of 24 °C). Figure 1b shows the typical current density-voltage (J-V) forward and reverse sweep characteristics of fresh and aged cells under the standard reporting condition, i.e., air mass 1.5 global (AM1.5G) at 1000 W m^{-2} and 25 °C, with the J-V curve parameters shown in the Supplemental Information. Clearly, a slow degradation mechanism impacts the electrical performance parameters of freshly prepared cells over time, with the biggest change occurring in the fill factor (FF). We will show later that changes in the IMPS features during this period are consistent with J-V curve parameter changes, and, hence, this technique provides a promising avenue for the effective monitoring of PSC degradation dynamics.

This study makes use of a modified version of the ECM proposed by Ravishankar et al.,[12] as shown in Figure 1c. Broadly speaking, two frequency domains are used in our model. The low frequency (LF) domain generally spans from 1 Hz to 1 kHz, and the high frequency (HF) regime is usually

associated with frequencies greater than 1 kHz. The equivalent circuit model incorporates an HF resistance (R_{HF}), sometimes known as the recombination resistance, in parallel with the branch R_{LF}-C_{LF}, where R_{LF} and C_{LF} denote an LF resistance and capacitance, respectively.

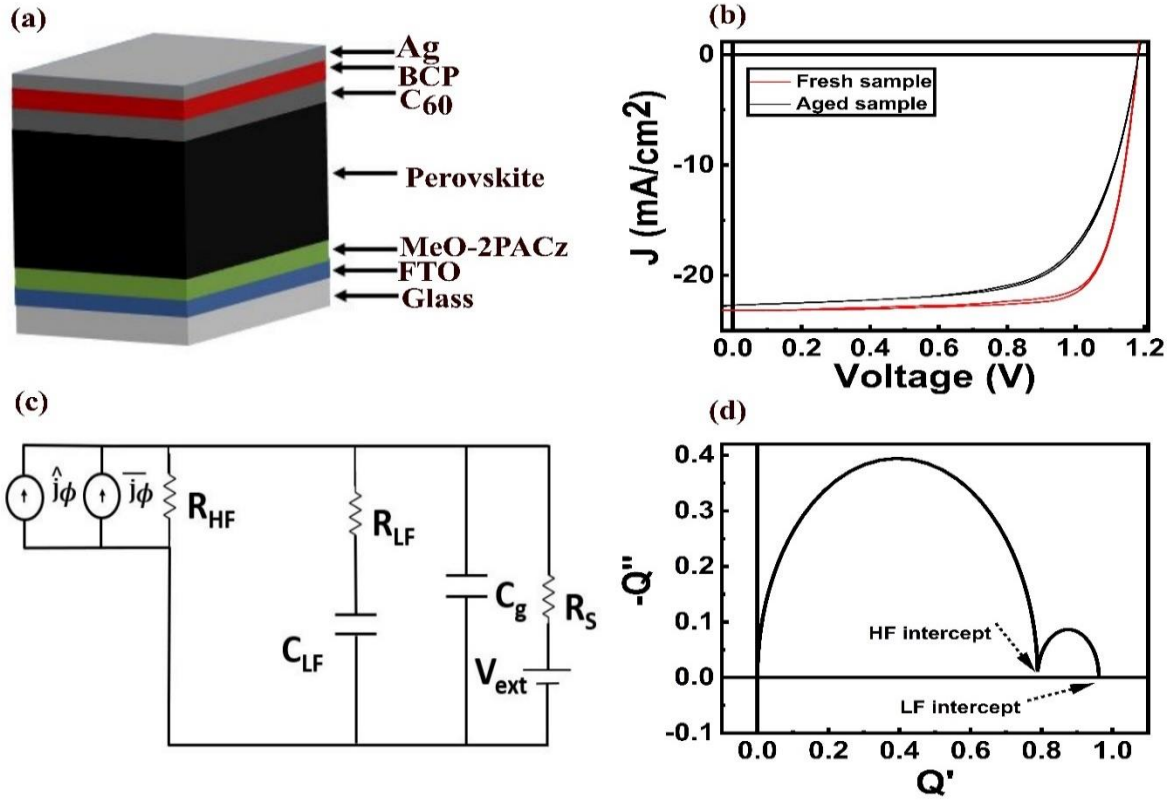

Figure 1 (a) Solar cell device structure (silver (Ag)/bathocuproin (BCP)/C_{60}/perovskite ($Cs_{0.05}$ $Rb_{0.05}$ $MA_{0.05}$ $FA_{0.85}$ $PbI2_{2.85}$ $Br_{0.15}$)/2-(3,6-Dimethoxycarbazol-9-yl)ethylphosphonic acid (MeO-2PACz)/FTO/Glass), (b) J-V curves for fresh and aged cells, (c) equivalent circuit model used to analyze the results in this work, and (d) an example Q-plane plot of the IMPS transfer function based on the ECM in (c).

This R_{LF}-C_{LF} branch is mainly responsible for the smaller arc feature in the upper quadrant observed in the Q-plane plot, as shown in Figure 1d. These elements are shunted by a high-frequency capacitance, also known as the geometric capacitance (C_g). Lastly, a large arc at high frequencies is formed and is mostly due to the coupling strength between the series resistance (R_s), the $R_{HF,}$ and the C_g. Based on the equivalent circuit model as shown in Figure 1c, the IMPS transfer function Q can be derived as:

$$Q = (1 + \frac{R_s}{R_{HF}} + i\omega R_S \mathrm{Cg} + \frac{1}{\frac{R_{LF}}{R_S} + \frac{1}{i\omega R_S C_{LF}}})^{-1} \quad (1)$$

where $\omega = 2\pi f$ is the angular frequency and i is the imaginary unit. The derivation of Eq. 1 is shown in the Supplemental Information, section S2. This model for the transfer function predicts one smaller LF arc and one larger HF arc both in the upper quadrant. The Q′ intercepts of the Q function, as marked in Figure 1d, are also interesting quantities to take note of:

$$\text{HF intercept} = (1 + R_s[\frac{1}{R_{HF}} + \frac{1}{R_{LF}}])^{-1} \quad (2a)$$

$$\text{LF intercept} = (1 + \frac{R_S}{R_{HF}})^{-1} \quad (2b)$$

Since these intercepts shift along the Q′ axis depending on various device stressors (i.e., bias light, voltage bias, etc.), monitoring the intercepts can quickly provide insights into how these stressors are affecting the carrier dynamics within the cell stack.

We note that the original ECM proposed by Ravishankar et. al. contains an additional resistance and capacitance parallel branch in series with R_{HF}. This additional branch leads to another low frequency arc in the lower Q′-Q″ quadrant and has traditionally been associated with ionic-electronic charging at the interfaces. This arc has also been related to artifacts of measuring instruments.[25,26] Although this third low frequency arc has been reported in most previous PSC IMPS studies, we do not observe it in our high efficiency solar cells and will therefore only use the modified, double-arc ECM to interpret our measurement results. We speculate that high efficiency PSCs do not suffer from slower ionic species that impede charge transfer through interfaces and have been associated with the 3rd low frequency arc often reported in low efficiency solar cells.[12,16,25]

Figure 2 illustrates a set of IMPS measurements with an ultralow intensity modulated 532 nm sinusoidal excitation (E_{AC} = 0.0043 mW cm^{-2} root mean square (RMS) intensity for all data reported in this work, see Supplemental Information Section S1.4), and IMPS measurements that add a series of progressively larger steady-state light biases (from a 632 nm LED), for a fresh cell and after 8 weeks. Here, we show both the Q′-ω and -Q″-ω frequency Bode plots and the corresponding Q′-Q″ plots to provide a complete picture. Focusing first on the E_{DC} = 0 mWcm^{-2} (no LB) data from the fresh cell (Figure 2a-c), the 3 IMPS plots exhibit a small, low frequency feature that tends to diminish under the influence of light bias.

Nevertheless, over a span of 8 weeks, this feature becomes progressively more pronounced such that a greater amount of LB is needed to suppress it, as shown in Figure 2d-f. In Figure 2(a & d), Q′, which in the $\omega \rightarrow 0$ limit corresponds to the differential EQE of the cell, shows one small 'step-down' feature at $\omega \approx 200$ Hz and another large one at $\omega \approx 1$ MHz, corresponding to two local maxima in the -Q″-ω plot (Fig. 2(b & e)). These two distinct features correspond to one small and one large arc in the Q-plane plot in Fig. 2 (c & f), although the larger arc requires frequencies higher than 1 MHz to be fully mapped. Both arcs are situated within the upper quadrant.

In most previous IMPS studies[12,27] in PSCs, a low-frequency arc in the lower quadrant (+Q′, +Q″) is also reported, but such an arc is absent in our devices, as mentioned previously, indicating that ion-mediated capacitive effects are not noticeably present in these high-efficiency devices, at least down to a frequency of 1 Hz that we have used to study the IMPS response in these cells. Focusing on the black symbols corresponding to a measurement with no added LB, the two visible arcs are indicative of two different relaxation times for charge carriers that are transported through the device stack.[28 24]

With the addition of a remarkably small amount of LB (E_{DC} = 0.017 mW/cm^2), we immediately observe a reduction in the Q′ step size in the low-frequency region. With the fresh cell, additional LBs have minimal further impact on the step size, but as the cell degrades over time, progressively larger amounts of LBs are required to reduce and flatten out the step. For example, the 8-week old cell reaches the LB saturation point at an intensity of 0.078 mW/cm^2. In the Q′-Q″ plot, whether fresh or aged, the LF intercept shifts to the left (lower Q′), and the size (defined as the width of the

arc that is given by the distance of its intercepts on the Q′ axis) of the arc is reduced substantially until it reaches a saturation point and does not change with more light bias.

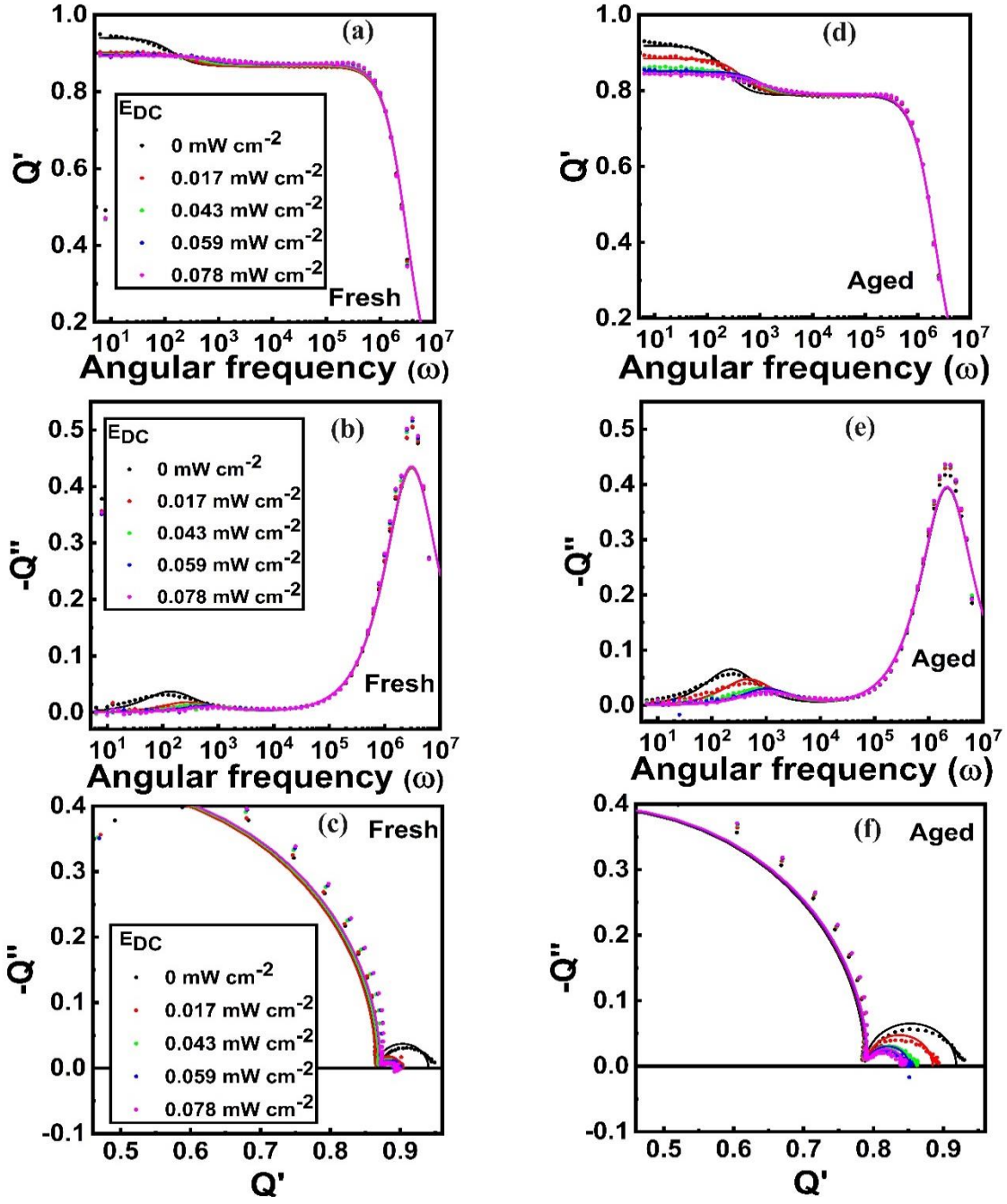

Figure 2 (a) Real part of the IMPS signal (Q′ transfer function) as a function of the angular frequency ω for several dc light bias intensities in a fresh cell. (b) Imaginary part of the IMPS signal (Q″) vs. ω (fresh cell) and (c) the Q′-Q″ plot for the LB intensities shown (fresh cell). The symbols represent the experimental data and the solid lines are the best fits to the data based on the ECM model of Eq. 1. (d-f) IMPS response of the same cell after 8 weeks of aging. E_{AC} = 0.0043 mW cm^{-2} for all measurements.

At the same time, in the ω ≈ 200 Hz range, the -Q″ local maximum shifts to higher frequencies. Finally, the high-frequency region shows very little change with LB, and the large arc in the Q-

plane plot remains at approximately the same magnitude. Figure S3 in the Supplemental Information shows the full high frequency arc. This high-frequency signal is attributed to the time-delayed capacitive discharge of the geometrical capacitor formed by the whole perovskite device stack and the contacts,[23,28,29] a process clearly unaffected by the addition of LB-induced charge carrier generation in the active layer.

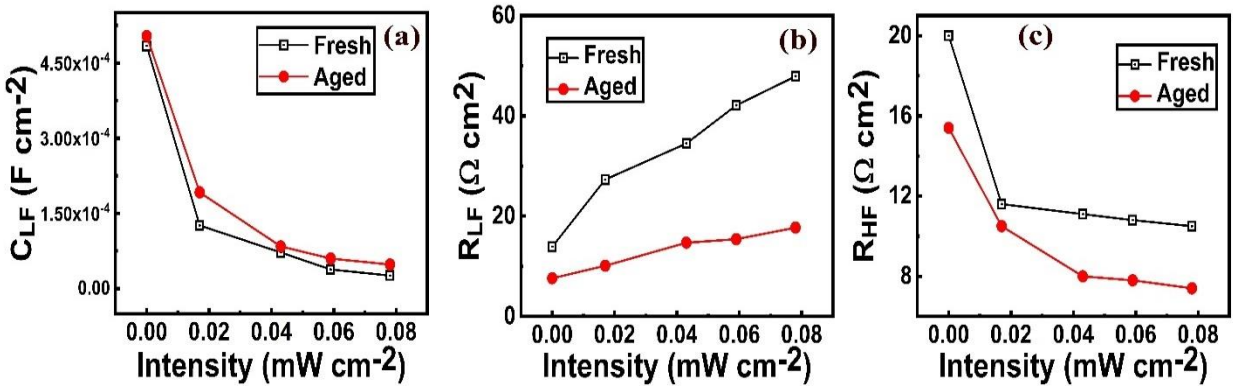

Figure 3 Extracted ECM parameters as a function of light intensity for the fresh and the aged cells: (a) low frequency capacitance, C_{LF}, (b) low frequency resistance, R_{LF} (c) and the high frequency resistance, R_{HF}.

For further insight into these results, all of the experimental IMPS features (from fresh devices and after 8 weeks of aging) were fitted to the ECM described above, and the best-fit parameters were extracted as shown in the Supplemental Information (Table S1 and Table S2). The evolution of C_{LF}, R_{LF}, and R_{HF} as a function of light bias intensity for both the fresh and the aged cells is shown in Figure 3, while C_g and R_s are kept fixed. Here, we simultaneously fit all 3 plots of Q′-ω, -Q″-ω, Q′-Q″ to the ECM model since the individual fitting of each one will not ensure a consistent and universal set of fit parameters. The IMPS responses characterized by the LF arcs are predominantly influenced by the interplay of C_{LF}, R_{LF}, and R_{HF}.[12] For this LB IMPS series, the ECM shows that as LB intensity increases, C_{LF} decreases, R_{LF} increases, and R_{HF} decreases by a similar amount. R_{HF}, generally associated with bulk recombination resistance, is reduced under light bias due to increased recombination losses in the bulk,[12] but soon reaches a steady state. This reduction in R_{HF} is what causes the LF intercept to shift to the left in Figure 2 (c & f), and Eq. 2b also predicts this shift. However, the most interesting observation in Figure 2, i.e., the reduction in size of the LF arc in the Q′-Q″ plot, comes from the decrease in C_{LF} and the increase in R_{LF} as LB intensity is increased.

Various explanations have been put forth on the origin of the LF arc. Some works have speculated that the LF feature is the result of the accumulation of anions and electrons at the perovskite/HTL interface.[12,19] However, others point to a multiple-trapping model of charge carriers within the device as being the most consistent with the intensity or wavelength dependence of the LF IMPS response.[29,30] Previous current-voltage modeling work[31] has shown that charge carrier trapping at grain boundaries and perovskite/transport layer interfaces can contribute to significant recombination losses in the cell. It is believed that electron trap states (mostly likely formed by halide vacancies) are positively charged when empty but become neutral when filled, and hence, their effect on carrier transport is weakened, corresponding to decreased C_{LF} and increased R_{LF}. Therefore, it is likely that with bias light, these traps are filled and become less active, causing the

LF arc to become smaller. The significant reduction of the C_{LF} with LB and the increase in R_{LF} suggest that the influence of that branch of the ECM on the device current is reduced, consistent with a general reduction on the influence of traps as LB is applied to the cell.

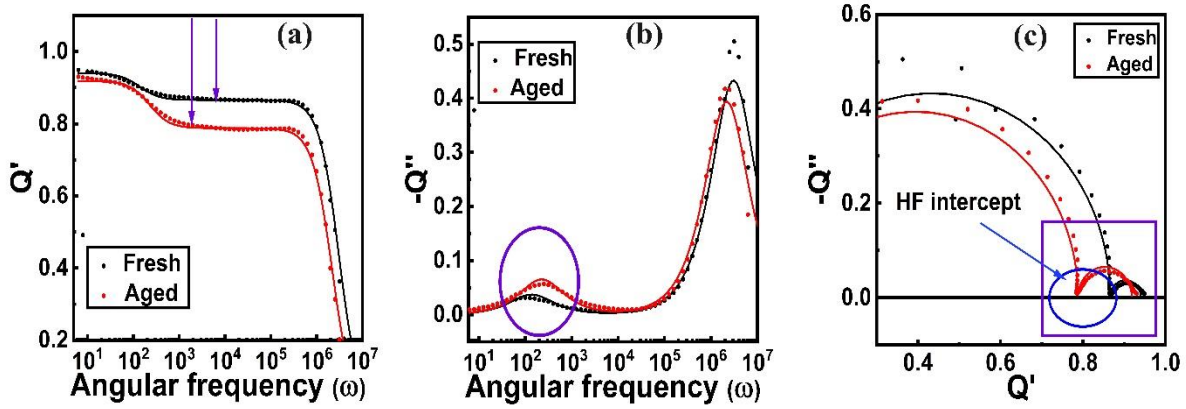

Figure 4 Comparing (a) Q′-ω plots, (b) Q″-ω plots and (c) Q-plane plots of the fresh and the 8-week-old cell under no LB. The symbols represent the experimental data, and the solid lines are the best fits to the data based on the ECM model of Eq. 1. E_{AC} = 0.0043 mW cm^{-2} and E_{DC} = 0 mW cm^{-2} for all measurements.

In addition to electronic charges, influence of ion migration in the frequency range from 10 Hz to 10^3 Hz cannot be completely ignored. Based on simulation by Schiller et al.[32], although most slow ions only respond to low frequency (<1 Hz) perturbation, some fast mobile ions (5×10^{-8} to 5×10^{-7} cm^2/Vs) can contribute to the capacitive response in this low frequency range. For perovskite solar cells, fast ions show an average diffusion coefficient of up to 10^{-6} cm^2/Vs,[33] which is sufficient to have an influence on the low frequency arc. Furthermore, some previous works suggest that the LB can enhance the ion migration.[34,35] These migrating ions may heal the defect/trap states at the interfaces or the bulk, resulting in reduced recombination rates.[36] Therefore, we speculate that a combination of mobile ions and free charge carriers are responsible for the trap filling effects we have observed in our measurements.

It should be emphasized again that the small LF arc observed in these devices is only detected because of the use of a very small-amplitude excitation source. Changing the modulation amplitude to a higher value substantially reduces or eliminates the LF arc as shown in the Supplemental Information (Figure S4) and leaves only the HF arc. A higher modulation intensity is equivalent to applying light bias to the cell and as we have shown in this work, light bias passivates the impact of traps on charge transport. This finding contrasts with previous work[17] where excitation or light bias intensities well in excess of 1 mW cm^{-2} have been utilized. This finding indicates that these devices do not suffer from a large number of trap states, although determining the trap energy levels and concentration likely requires additional detection techniques such as deep level transient spectroscopy, which is beyond the scope of this work.

We examine the fresh versus the 8-week degraded cell's IMPS features more closely in Figure 4 (a-c) by showing the pre- and post-degradation Q′ vs ω, -Q″ vs ω, and Q′-Q″ plots together for the no LB case. Recently, degradation studies in PSCs have garnered a lot of attention [37–39]. It can be clearly seen in Figure 4 that a slow degradation occurs over time, affecting the LF arc, with both the HF and the LF intercepts shifting to the left. However, the LF intercept shift is significantly smaller than the HF intercept shift, as seen in the Q-plane plots (Figure 4(c)). In the

ECM, the LF intercept is dictated by changes in the R_{HF}, whereas the HF intercept is affected by changes to both the R_{HF} and R_{LF} elements.

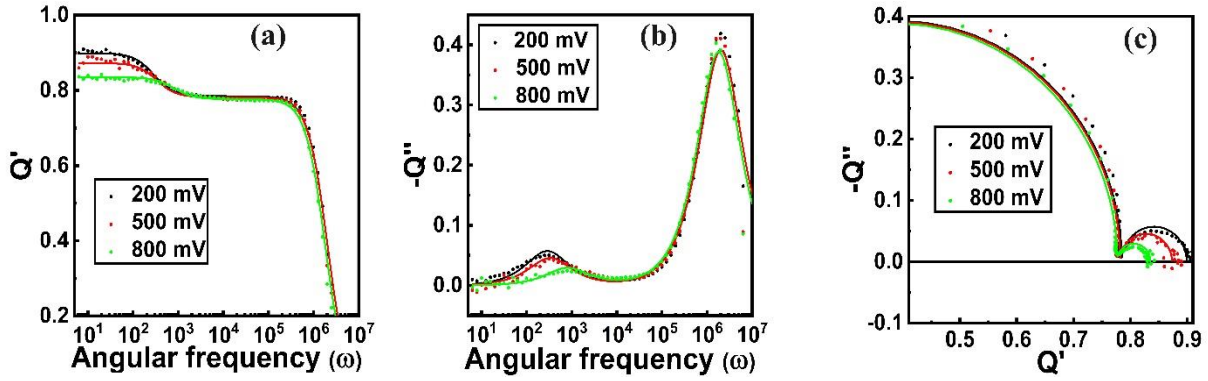

Figure 5 (a) Real part of the IMPS signal (Q′ transfer function) as a function of the angular frequency ω for several dc voltage biases. (b) Imaginary part of the IMPS signal (Q″) vs ω. (c) The Q′-Q″ plot for the bias voltages shown. The symbols represent the experimental data, and the solid lines are the best fits to the data based on the ECM model of Eq. 1. The data is for the 8-week-old cell. E_{AC} = 0.0043 mW cm^{-2} and E_{DC} = 0 mW cm^{-2} for all measurements

Therefore, the small shift in the LF intercept indicates that the bulk recombination resistance, R_{HF}, has not reduced much over 8 weeks. However, R_{LF} has been reduced more substantially over this timeframe, which causes a bigger shift in the HF intercept. Also, the decrease in the R_{LF} is one reason the size of the LF arc has increased, corresponding to a larger step-down feature in the Q′-ω plot and a larger local maximum in the Q″-ω plot. Since we have associated the LF arc as a trap related feature, we can speculate that the density of these particular traps (whether interfacial or bulk is not clear) in the device increases over time.

Furthermore, we believe that the large reduction in the R_{LF} value of the aged cell is correlated with the significant reduction of the fill factor observed by measuring its J-V curve. Under the largest light bias, the R_{LF} becomes the dominant resistor element in the ECM, and the larger its value, the more effective the cell becomes at preventing a current loss through the LF branch of the circuit during a J-V sweep. For the aged cell, this current blocking is not as effective, leading to a deterioration of the fill factor. A similar observation was reported previously among several perovskite cells exhibiting different J-V curve characteristics[12].

Table 1 ECM parameters obtained from fitting the 8-week-old cell IMPS data under different voltage biases

Voltage bias	200 mV	500 mV	800 mV
C_{LF} (F/cm^2)	3.4×10^{-4}	2.5×10^{-4}	6.4×10^{-5}
R_{LF} (Ω cm^2)	8.9	10.8	18.1
R_{HF} (Ω cm^2)	12.8	9.9	8.2
C_g (F/cm^2)	4.4×10^{-7}	4.4×10^{-7}	4.4×10^{-7}
R_S (Ω cm^2)	1.4	1.4	1.6

Finally, a series of IMPS measurements were conducted under varying forward voltage biases, from 200 mV to 800 mV, as shown in Figure 5. The same two arcs were observed in the upper quadrant, with similar characteristics to the light bias case; i.e., the LF arc amplitude reduces with

applied V, and the LF intercept shifts to the left. Since applied voltage in the forward bias direction causes carrier injection into the cell from the contacts, it is likely that these extra carriers increase recombination in the bulk (reducing R_{HF}) and help with filling some of the empty traps at either the interfaces or within the bulk grain boundaries (increasing R_{LF}). Therefore, a similar shrinking of the LF arc that took place in the LB case is expected here. The ECM model of Figure 1 was fit to the voltage bias series, with the model calculations shown as solid lines in Figure 5. Table 1 shows the best-fit parameters of the bias voltage series, and a pattern very similar to the LB series emerges here as well: the C_{LF} capacitance decreases, and the R_{LF} resistance increases as the voltage bias is increased, indicating a decrease in the role of the underlying traps on the transport of charge carriers across the device layers.

In summary, ultralow intensity modulation with superimposed light bias, also in low intensity, and voltage bias, was used to extract the IMPS transfer function for a high-efficiency perovskite solar cell. A small light bias-dependent arc in the upper quadrant of the Q-plane is shown to be consistent with a trap-assisted capacitive discharge within the cell. This LF arc grows more pronounced over time when the cell slowly degrades in the lab environment, even when not under combined active environmental stressors. These IMPS features can be successfully reproduced with the utilization of a suitable ECM. The employment of this modeling framework facilitated the explanation of different kinetic processes within the device. Our work indicates that IMPS features, such as shifts in the LF and HF intercepts, along with the size of the observed Q-plane arcs can be useful in accessing the quality of freshly fabricated cells and also in monitoring the effect of degradation on trap or defect formation inside the solar cell structure.

ASSOCIATED CONTENT

Supporting Information

Description of experimental section, additional experimental results

Notes

The authors declare no competing financial interest.

Acknowledgments

Z.S. and Y.Y. acknowledge funding support from the U.S. Air Force Research Laboratory, Space Vehicles Directorate, Under Contract #FA9453-19-C-1002.

REFERENCES

(1) Kim, G. H.; Kim, D. S. Development of Perovskite Solar Cells with >25% Conversion Efficiency. *Joule* **2021**, *5* (5), 1033–1035. https://doi.org/10.1016/j.joule.2021.04.008.

(2) Haider, S. Z.; Anwar, H.; Wang, M. Theoretical Device Engineering for High-Performance Perovskite Solar Cells Using CuSCN as Hole Transport Material Boost the Efficiency Above 25%. *physica status solidi (a)* **2019**, *216* (11), 1900102. https://doi.org/10.1002/pssa.201900102.

(3) Lin, Z.; Xu, X.; Dong, H.; Song, Q.; Duan, H.; Mu, C. Enhancing the Efficiency of Perovskite Solar Cells by Bidirectional Modification of the Perovskite and Electron Transport Layer. *ACS Appl Mater Interfaces* **2023**, *15* (1), 1097–1104. https://doi.org/10.1021/acsami.2c18341.

(4) Chowdhury, T. A.; Bin Zafar, M. A.; Sajjad-Ul Islam, M.; Shahinuzzaman, M.; Islam, M. A.; Khandaker, M. U. Stability of Perovskite Solar Cells: Issues and Prospects. *RSC Adv* **2023**, *13* (3), 1787–1810. https://doi.org/10.1039/D2RA05903G.

(5) Mazumdar, S.; Zhao, Y.; Zhang, X. Stability of Perovskite Solar Cells: Degradation Mechanisms and Remedies. *Frontiers in Electronics* **2021**, *2* (August), 1–34. https://doi.org/10.3389/felec.2021.712785.

(6) Zai, H.; Ma, Y.; Chen, Q.; Zhou, H. Ion Migration in Halide Perovskite Solar Cells: Mechanism, Characterization, Impact and Suppression. *Journal of Energy Chemistry* **2021**, *63*, 528–549. https://doi.org/10.1016/j.jechem.2021.08.006.

(7) Kundu, S.; Kelly, T. L. In Situ Studies of the Degradation Mechanisms of Perovskite Solar Cells. *EcoMat* **2020**, *2* (2). https://doi.org/10.1002/eom2.12025.

(8) Zheng, X.; Wang, X.; Li, W.; Liu, Z.; Ming, W.; Wang, H.; Wang, H.; Li, D.; Liu, B.; Yang, C. Correlations of Ionic Migration and Deep-Level Traps Leads to Surface Defect Formation in Perovskite Solar Cells. *The Journal of Physical Chemistry C* **2021**, *125* (35), 19551–19559. https://doi.org/10.1021/acs.jpcc.1c05519.

(9) Roose, B. Ion Migration Drives Self-Passivation in Perovskite Solar Cells and Is Enhanced by Light Soaking. *RSC Adv* **2021**, *11* (20), 12095–12101. https://doi.org/10.1039/d1ra01166a.

(10) Moghadamzadeh, S.; Hossain, I. M.; Jakoby, M.; Abdollahi Nejand, B.; Rueda-Delgado, D.; Schwenzer, J. A.; Gharibzadeh, S.; Abzieher, T.; Khan, M. R.; Haghighirad, A. A.; Howard, I. A.; Richards, B. S.; Lemmer, U.; Paetzold, U. W. Spontaneous Enhancement of the Stable Power Conversion Efficiency in Perovskite Solar Cells. *J Mater Chem A Mater* **2020**, *8* (2), 670–682. https://doi.org/10.1039/C9TA09584E.

(11) Shi, J.; Li, Y.; Li, Y.; Li, D.; Luo, Y.; Wu, H.; Meng, Q. From Ultrafast to Ultraslow: Charge-Carrier Dynamics of Perovskite Solar Cells. *Joule* **2018**, *2* (5), 879–901. https://doi.org/10.1016/j.joule.2018.04.010.

(12) Ravishankar, S.; Riquelme, A.; Sarkar, S. K.; Garcia-Batlle, M.; Garcia-Belmonte, G.; Bisquert, J. Intensity-Modulated Photocurrent Spectroscopy and Its Application to Perovskite Solar Cells. *Journal of Physical Chemistry C* **2019**, *123* (41), 24995–25014. https://doi.org/10.1021/acs.jpcc.9b07434.

(13) Pockett, A.; Spence, M.; Thomas, S. K.; Raptis, D.; Watson, T.; Carnie, M. J. Beyond the First Quadrant: Origin of the High Frequency Intensity-Modulated Photocurrent/Photovoltage Spectroscopy Response of Perovskite Solar Cells. *Solar RRL* **2021**, *5* (5), 1–7. https://doi.org/10.1002/solr.202100159.

(14) Alvarez, A. O.; Ravishankar, S.; Fabregat-Santiago, F. Combining Modulated Techniques for the Analysis of Photosensitive Devices. *Small Methods* **2021**, *5* (10), 2100661. https://doi.org/10.1002/smtd.202100661.

(15) Bedoya-Lora, F. E.; Valencia-García, M. E.; Hankin, A.; Klotz, D.; Calderón, J. A. Determination of Photon-Driven Charge Transfer Efficiency: Drawbacks, Accuracy and Precision of Different Methods Using Hematite as Case of Study. *Electrochim Acta* **2022**, *402*, 139559. https://doi.org/10.1016/j.electacta.2021.139559.

(16) Bou, A.; Pockett, A.; Raptis, D.; Watson, T.; Carnie, M. J.; Bisquert, J. Beyond Impedance Spectroscopy of Perovskite Solar Cells: Insights from the Spectral Correlation of the Electrooptical Frequency Techniques. *Journal of Physical Chemistry Letters* **2020**, *11* (20), 8654–8659. https://doi.org/10.1021/acs.jpclett.0c02459.

(17) Ravishankar, S.; Aranda, C.; Boix, P. P.; Anta, J. A.; Bisquert, J.; Garcia-Belmonte, G. Effects of Frequency Dependence of the External Quantum Efficiency of Perovskite Solar Cells. *Journal of Physical Chemistry Letters* **2018**, *9* (11), 3099–3104. https://doi.org/10.1021/acs.jpclett.8b01245.

(18) Ghahremanirad, E.; Almora, O.; Suresh, S.; Drew, A. A.; Chowdhury, T. H.; Uhl, A. R. Beyond Protocols: Understanding the Electrical Behavior of Perovskite Solar Cells by Impedance Spectroscopy. *Adv Energy Mater* **2023**, *13* (30). https://doi.org/10.1002/aenm.202204370.

(19) Srivastava, P.; Kumar, R.; Ronchiya, H.; Bag, M. Intensity Modulated Photocurrent Spectroscopy to Investigate Hidden Kinetics at Hybrid Perovskite–Electrolyte Interface. *Sci Rep* **2022**, *12* (1), 1–13. https://doi.org/10.1038/s41598-022-16353-6.

(20) Parikh, N.; Pandey, M.; Kumar, M.; Prochowicz, D.; Kalam, A.; Tavakoli, M. M.; Satapathi, S.; Yadav, P. Identifying Dominant Recombination Mechanisms in Spiro-Based Conventional Perovskite Solar Cells: Roles of Interface and Bulk Recombination. *Energy Reports* **2022**, *8*, 7957–7963. https://doi.org/10.1016/j.egyr.2022.06.047.

(21) Laird, J. S.; Ravishankar, S.; Rietwyk, K. J.; Mao, W.; Bach, U.; Smith, T. A. Intensity Modulated Photocurrent Microspectrosopy for Next Generation Photovoltaics. *Small Methods* **2022**, *6* (9), e2200493. https://doi.org/10.1002/smtd.202200493.

(22) Bou, A.; Āboliņš, H.; Ashoka, A.; Cruanyes, H.; Guerrero, A.; Deschler, F.; Bisquert, J. Extracting in Situ Charge Carrier Diffusion Parameters in Perovskite Solar Cells with Light Modulated Techniques. *ACS Energy Lett* **2021**, *6* (6), 2248–2255. https://doi.org/10.1021/acsenergylett.1c00871.

(23) Ravishankar, S.; Aranda, C.; Sanchez, S.; Bisquert, J.; Saliba, M.; Garcia-Belmonte, G. Perovskite Solar Cell Modeling Using Light- and Voltage-Modulated Techniques. *Journal of Physical Chemistry C* **2019**, *123* (11), 6444–6449. https://doi.org/10.1021/acs.jpcc.9b01187.

(24) Jiang, Q.; Tong, J.; Xian, Y.; Kerner, R. A.; Dunfield, S. P.; Xiao, C.; Scheidt, R. A.; Kuciauskas, D.; Wang, X.; Hautzinger, M. P.; Tirawat, R.; Beard, M. C.; Fenning, D. P.; Berry, J. J.; Larson, B. W.; Yan, Y.; Zhu, K. Surface Reaction for Efficient and Stable Inverted Perovskite Solar Cells. *Nature* **2022**, *611* (7935), 278–283. https://doi.org/10.1038/s41586-022-05268-x.

(25) Ravishankar, S.; Garcia-Batlle, M.; Bisquert, J.; Garcia-Belmonte, G.; Odrobina, J.; Schiller, C.-A. Removing Instability-Caused Low-Frequency Features in Small Perturbation Spectra of Perovskite Solar Cells. *The Journal of Physical Chemistry C* **2020**, *124* (29), 15793–15799. https://doi.org/10.1021/acs.jpcc.0c04050.

(26) Alvarez, A. O.; Riquelme, A. J.; Fuentes-Pineda, R.; Mas-Marzá, E.; Marsal, L. F.; Almora, O.; Anta, J. A.; Fabregat-Santiago, F. Correcting Unintended Changes in Electroluminescence Perturbation for Reliable Light Intensity Modulated Spectroscopies. *Phys Scr* **2023**, *98* (8), 085525. https://doi.org/10.1088/1402-4896/ace4fc.

(27) Antuch, M. On the Evolution of the Intensity Modulated Photocurrent Spectroscopy (IMPS) Transfer Function in Quadrants (IV)-(I) or Quadrants (II)-(III). *Curr Opin Electrochem* **2022**, *35*, 101043. https://doi.org/10.1016/j.coelec.2022.101043.

(28) Pockett, A.; Eperon, G. E.; Peltola, T.; Snaith, H. J.; Walker, A.; Peter, L. M.; Cameron, P. J. Characterization of Planar Lead Halide Perovskite Solar Cells by Impedance Spectroscopy, Open-Circuit Photovoltage Decay, and Intensity-Modulated Photovoltage/Photocurrent Spectroscopy. *Journal of Physical Chemistry C* **2015**, *119* (7), 3456–3465. https://doi.org/10.1021/jp510837q.

(29) Riquelme, A.; Gálvez, F. E.; Contreras-Bernal, L.; Míguez, H.; Anta, J. A. Internal Quantum Efficiency and Time Signals from Intensity-Modulated Photocurrent Spectra of Perovskite Solar Cells. *J Appl Phys* **2020**, *128* (13). https://doi.org/10.1063/5.0013317.

(30) Todinova, A.; Idígoras, J.; Salado, M.; Kazim, S.; Anta, J. A. Universal Features of Electron Dynamics in Solar Cells with TiO 2 Contact: From Dye Solar Cells to Perovskite Solar Cells. *J Phys Chem Lett* **2015**, *6* (19), 3923–3930. https://doi.org/10.1021/acs.jpclett.5b01696.

(31) Sherkar, T. S.; Momblona, C.; Gil-Escrig, L.; Ávila, J.; Sessolo, M.; Bolink, H. J.; Koster, L. J. A. Recombination in Perovskite Solar Cells: Significance of Grain Boundaries, Interface Traps, and Defect Ions. *ACS Energy Lett* **2017**, *2* (5), 1214–1222. https://doi.org/10.1021/acsenergylett.7b00236.

(32) Neukom, M. T.; Schiller, A.; Züfle, S.; Knapp, E.; Ávila, J.; Pérez-del-Rey, D.; Dreessen, C.; Zanoni, K. P. S.; Sessolo, M.; Bolink, H. J.; Ruhstaller, B. Consistent Device Simulation Model Describing Perovskite Solar Cells in Steady-State, Transient, and Frequency Domain. *ACS Appl Mater Interfaces* **2019**, *11* (26), 23320–23328. https://doi.org/10.1021/acsami.9b04991.

(33) Tammireddy, S.; Reichert, S.; An, Q.; Taylor, A. D.; Ji, R.; Paulus, F.; Vaynzof, Y.; Deibel, C. Temperature-Dependent Ionic Conductivity and Properties of Iodine-Related Defects in Metal Halide Perovskites. *ACS Energy Lett* **2022**, *7* (1), 310–319. https://doi.org/10.1021/acsenergylett.1c02179.

(34) Li, Y.-T.; Ding, L.; Li, J.-Z.; Kang, J.; Li, D.-H.; Ren, L.; Ju, Z.-Y.; Sun, M.-X.; Ma, J.-Q.; Tian, Y.; Gou, G.-Y.; Xie, D.; Tian, H.; Yang, Y.; Wang, L.-W.; Peng, L.-M.; Ren, T.-L. Light-Enhanced Ion Migration in Two-Dimensional Perovskite Single Crystals Revealed in Carbon Nanotubes/Two-Dimensional Perovskite Heterostructure and Its Photomemory Application. *ACS Cent Sci* **2019**, *5* (11), 1857–1865. https://doi.org/10.1021/acscentsci.9b00839.

(35) Zhao, Y.-C.; Zhou, W.-K.; Zhou, X.; Liu, K.-H.; Yu, D.-P.; Zhao, Q. Quantification of Light-Enhanced Ionic Transport in Lead Iodide Perovskite Thin Films and Its Solar Cell Applications. *Light Sci Appl* **2016**, *6* (5), e16243–e16243. https://doi.org/10.1038/lsa.2016.243.

(36) Xiao, C.; Zhai, Y.; Song, Z.; Wang, K.; Wang, C.; Jiang, C.-S.; Beard, M. C.; Yan, Y.; Al-Jassim, M. Operando Characterizations of Light-Induced Junction Evolution in Perovskite Solar Cells. *ACS Appl Mater Interfaces* **2023**, *15* (17), 20909–20916. https://doi.org/10.1021/acsami.2c22801.

(37) Prasanna, R.; Leijtens, T.; Dunfield, S. P.; Raiford, J. A.; Wolf, E. J.; Swifter, S. A.; Werner, J.; Eperon, G. E.; de Paula, C.; Palmstrom, A. F.; Boyd, C. C.; van Hest, M. F. A. M.; Bent, S. F.; Teeter, G.; Berry, J. J.; McGehee, M. D. Design of Low Bandgap Tin–Lead Halide Perovskite Solar Cells to Achieve Thermal, Atmospheric and Operational Stability. *Nat Energy* **2019**, *4* (11), 939–947. https://doi.org/10.1038/s41560-019-0471-6.

(38) Baumann, F.; Raga, S. R.; Lira-Cantú, M. Monitoring the Stability and Degradation Mechanisms of Perovskite Solar Cells by in Situ and Operando Characterization. *APL Energy* **2023**, *1* (1). https://doi.org/10.1063/5.0145199.

(39) Zhang, D.; Li, D.; Hu, Y.; Mei, A.; Han, H. Degradation Pathways in Perovskite Solar Cells and How to Meet International Standards. *Commun Mater* **2022**, *3* (1), 58. https://doi.org/10.1038/s43246-022-00281-z.